RESEARCH ARTICLE

Quantitative susceptibility mapping of the head-and-neck using SMURF fat-water imaging with chemical shift and relaxation rate corrections

Beata Bachrata[1,2] 🔵 iD | Siegfried Trattnig[1,2] 🔵 iD | Simon Daniel Robinson[1,2,3,4] 🔵 iD 🐦

[1]High Field MR Centre, Department of Biomedical Imaging and Image-Guided Therapy, Medical University of Vienna, Vienna, Austria

[2]Karl Landsteiner Institute for Clinical Molecular MR in Musculoskeletal Imaging, Vienna, Austria

[3]Centre of Advanced Imaging, University of Queensland, Brisbane, Australia

[4]Department of Neurology, Medical University of Graz, Graz, Austria

Correspondence
Simon Daniel Robinson, High Field
Magnetic Resonance Centre, Medical
University of Vienna, Lazarettgasse 14,
A-1090 Wien, Austria.
Email: simon.robinson@meduniwien.
ac.at

Funding information
Bundesministerium für Digitalisierung
und Wirtschaftsstandort; H2020 Marie
Skłodowska-Curie Actions, Grant/
Award Number: MS-fMRI-QSM 794298;
Österreichische Nationalstiftung
für Forschung, Technologie und
Entwicklung; Austrian Science Fund,
Grant/Award Number: FWF 31452

Purpose: To address the challenges posed by fat-water chemical shift artifacts and relaxation rate discrepancies to quantitative susceptibility mapping (QSM) outside the brain, and to generate accurate susceptibility maps of the head-and-neck at 3 and 7 Tesla.

Methods: Simultaneous Multiple Resonance Frequency (SMURF) imaging was extended to 7 Tesla and used to acquire head-and-neck gradient echo images at both 3 and 7 Tesla. Separated fat and water images were corrected for Type 1 (displacement) and Type 2 (phase discrepancy) chemical shift artefacts, and for the bias resulting from differences in T_1 and T_2^* relaxation rates, recombined and used as the basis for QSM. A novel phase signal-based masking approach was used to generate head-and-neck masks.

Results: SMURF generated well-separated fat and water images of the head-and-neck. Corrections for chemical shift artefacts and relaxation rate differences removed overestimation of the susceptibility values, blurring in the susceptibility maps, and the disproportionate influence of fat in mixed voxels. The resulting susceptibility maps showed high correspondence between the paramagnetic areas and the locations of fatty tissues and the susceptibility estimates were similar to literature values. The proposed masking approach was shown to provide a simple means of generating head-and-neck masks.

Conclusion: Corrections for Type 1 and Type 2 chemical shift artefacts and for fat-water relaxation rate differences, mainly in T_1, were shown to be required for accurate susceptibility mapping of fatty-body regions. SMURF made it possible to apply these corrections and generate high-quality susceptibility maps of the entire head-and-neck at both 3 and 7 Tesla.

1 | INTRODUCTION

Quantitative susceptibility mapping (QSM) is a method for calculating the distribution of the magnetic susceptibilities of tissue from a fieldmap (ΔB_0)—the difference between the externally applied magnetic field and the demagnetisation field generated by the tissue itself.[1] The phase of the gradient-echo (GRE) signal is used to generate the fieldmap, which is converted to a map of susceptibility by removal of background fields and dipole inversion. Generation of an accurate fieldmap is a crucial step in the process, as errors generally propagate throughout the QSM analysis pipeline and bias susceptibility estimates.[2]

QSM provides excellent contrast in the imaging of calcifications, hemorrhages, and iron depositions, as well as tissue microstructure and oxygenation.[3] The technique has found application including the assessment of Alzheimer and Parkinson disease, Multiple Sclerosis (MS), the grading of tumors and monitoring of their growth,[4-6] and the past decade has seen an increase of interest in QSM outside the brain: in the liver,[7-11] breast,[3,12,13] kidney,[14] prostate,[15-17] heart,[18-20] knee,[21] trabecular bone,[22] spine,[23] and the entire head-and-neck region.[24-29] Compared to brain-only QSMs, susceptibility mapping of the head-and-neck allows the visualization of deep gray matter nuclei in the brainstem[30]—potential targets for deep brain stimulation[31,32]—MS lesions[33] in the brainstem, and visualization and assessment of tumors in the facial skull; epi-, naso-, and oropharynx; the base of the tongue and mouth; salivary glands; and possible regional lymph nodes.[34] The presence of fat in these regions, however, generally results in errors in field estimation that originate in several effects. First, because of the circa 3.4 ppm[35] chemical shift difference between fat and water, the fat image is shifted relative to water along the frequency-encoding direction by a number of voxels given by

$$N_{voxels} = \frac{\Delta f}{rBW/pixel},$$

where $rBW/pixel$ is the receiver bandwidth per pixel and Δf the fat-water chemical shift. This so-called Type 1 (displacement) chemical shift artifact (CSA) leads, in addition to the errors in the spatial distribution of susceptibility sources, also to areas of signal voids, making spatial phase-unwrapping problematic. While QSM generally benefits from the use of higher field strengths, allowing either shorter acquisition times or higher resolution,[36] the increased fat-water

chemical shift difference leads to a more pronounced Type 1 CSA. Second, the different precession frequency of fat with respect to water gives rise to an echo time (TE)-dependent phase component (φ) in GRE, defined as:

$$\Delta\varphi(TE) = 2\pi\Delta fTE,$$

which does not reflect the tissue susceptibility and also causes destructive interference between water and fat signals—the so-called Type 2 (phase discrepancy) CSA. Last, differences in T_1 and T_2^* relaxation times lead the acquired water and fat signals to be weighted differently, according to the signal equation:

$$S = \frac{PD\left(1 - e^{-TR/T_1}\right)e^{-TE/T_2^*}\sin\alpha}{1 - e^{-TR/T_1}\cos\alpha},$$

with PD being the proton density and α the flip angle (FA). The proton density ratio of the contributing water-based and fat-based tissues is biased by this signal weighting, which skews field estimates in mixed voxels.

To reduce the effects of Type 1 CSA, high receiver bandwidths are conventionally used, allowing only a partial correction and coming at the price of decreased SNR. To reduce Type 2 CSA, an acquisition at the in-phase TEs can be used,[12,23,24,26] although this restricts the choices of TEs. The effects of relaxation time differences are known to bias the estimation of proton density fat-fraction (PDFF),[37,38] but are generally neglected in QSM.[12,23,24,28] To minimize the bias caused by T_1 relaxation rate differences, small FAs have to be used, resulting in poor SNR, or a correction based on known T_1 values[38] can be applied. In the case of PDFF mapping of the iron overloaded liver, the differences in T_2^* are assumed to be negligible[39] due to the shortening of the values being dominated by the presence of iron. It remains to be established if this assumption holds in other cases or if a correction should be applied.

As an alternative to in-phase imaging, the Dixon approach[40] can be used, allowing the simultaneous generation of water-only and fat-only images from a multi-echo acquisition. Unlike in-phase imaging, Dixon allows PDFF maps to be generated simultaneously and the multi-peak fat spectrum to be considered. The Dixon approach is, however, problematic in voxels with fat-fractions close to 50%,[23] which may occur either in mixed tissues such as the parotid glands or, due to partial volume effects, at the edges of water-based and fat-based structures. The Dixon approach also requires a very short echo spacing to achieve robust fat-water separation,[41,42] which is suboptimal for

QSM, where the maximal contrast-to-noise ratio (CNR) is achieved at the TE close to the T_2^* of the tissue.[43] To overcome this problem and also the problem over-smoothing of the fieldmaps inherent to most of the Dixon approaches, two methods have been developed specifically for Dixon-based susceptibility mapping. The first method, simultaneous phase unwrapping and removal of chemical shift (SPURS),[9] simultaneously unwraps the phase and removes chemical shift using single species fitting combined with graph cuts, while the second technique uses two trains of echoes with short and long echo spacings.[44] However, none of the Dixon methods addresses the errors in susceptibility estimates resulting from Type 1 (displacement) CSA. In magnitude Dixon imaging, the separated water and fat images can be corrected for their relative displacement, allowing the generation of chemical shift displacement-free recombined fat-water images. The fieldmap, however, is generally generated as a by-product of the minimization step and, because Type 1 CSA affects the acquired multi-echo signal that is being fitted, it is present in the fieldmaps, to the detriment of QSM. The same is true for the in-phase imaging approach.

We have recently presented a Simultaneous Multiple Resonance Frequency (SMURF[45]) approach to fat-water imaging based on multi-band principles, which was applied to correct the CSAs in GRE and turbo spin-echo magnitude imaging at 3 T. In SMURF, multi-band pulses are applied together with CAIPIRINHA to allow separate images of fat and water to be generated. Prior to recombination, a complex summation of the fat and water signals, those signals can be corrected for Type 1 and Type 2 CSAs, and, if the relaxation times are known, for the bias resulting from fat-water relaxation rate differences. We hypothesized that the SMURF technique would yield similarly cleanly separated fat and water images at higher field strengths, as both field inhomogeneity and chemical shift difference generally scale with the field. Although a single-peak fat signal model is assumed in generating the spectrally selective radiofrequency (RF) pulses in SMURF, it has been shown that this approximation does not lead to significant bias in QSM outside the brain.[23] Susceptibility values of fatty tissues vary, however, quite widely in the literature,[23] e.g., 0.29 ppm[7] and 0.57 ppm[9] for the fat in the liver, 0.19 ppm[21] for the fat in the knee, and 0.29 ppm[24] for the fatty fascia in the head-and-neck. Nevertheless, in all cases was the fat assessed as being more paramagnetic than the surrounding water-based tissues.

In addition to the complications caused by the presence of fat, QSM outside the brain is also made problematic by the difficulties in generating the tissue masks required by most QSM approaches. Unlike for the brain, there are no standard segmentation tools, and simple magnitude thresholding generally includes some voxels with unreliable phase, giving rise to artifacts in the susceptibility maps, and potentially excludes extended areas of interest where coil sensitivities are low (e.g., in the neck at brainstem at a field strength of 7 T and above). Even these low signal areas often show high coherence of the phase signal, however. This, and the fact that magnitude-based masks include voxels with high magnitude signal but unreliable phase (e.g., veins) have led to the suggestion to generate masks using phase image.[46]

The aim of this study was to address the challenges of QSM outside the brain and, using simultaneous fat-water imaging with SMURF, to generate chemical shift and relaxation rate bias-free, high CNR susceptibility maps of the entire head-and-neck region. Since QSM generally benefits from the use of higher field, we extended SMURF to 7 T, although the need for different RF excitation pulses and the modified field variations this a non-trivial translation. Additionally, we aimed to develop a simple but robust approach for generating head-and-neck masks using the signal phase.

2 | METHODS

Measurements were performed with a 3T Siemens Prisma scanner (*syngo* MR VE11C, Siemens Healthineers, Erlangen, Germany) and a 7T Siemens MAGNETOM Plus scanner (*syngo* MR VE12U AP01). The head-and-neck region of 10 healthy volunteers was scanned—five volunteers at 3 T (V1–V5) using a 64-channel Siemens head-and-neck coil and five at 7 T (V6-V10) using a 32-channel head coil (Nova Medical, Wilmington, Massachusetts, USA). The 3T and 7T data were acquired to evaluate the performance of SMURF imaging at each field strength independently and to assess the effectiveness of the corrections for chemical shift and relaxation rate biases at the most commonly used field strengths in QSM, but not with the intention of comparing results between the two field strengths. Written informed consent was provided by all the participants, and the study was approved by the Ethics Committee of the Medical University of Vienna.

2.1 | RF pulse design

Least-squares-filtered minimum-phase Shinnar-Le Roux pulses[47-49] were designed using Vespa[50,51] and used to create both bands of two dual-band pulses: one optimized for fat-water imaging at 3 T[45] and one for 7 T.[29] The larger chemical shift difference at 7 T allowed the use of broader and, hence, shorter minimum-phase SLR RF pulses with a duration of 8.0 ms compared to 11.8 ms at 3 T, allowing a first echo time of about 2.5–4.5 ms at 7 T compared to about 4.5–7.0 ms at 3 T.

2.2 | Acquisition parameters

2.2.1 | 3T measurements

Sagittal 3D multi-echo GRE SMURF images were acquired with anterior-posterior phase-encoding direction, field of view (FOV) = 230 × 230 mm, resolution = 1.3 × 1.3 × 1.3 mm, 128 slices, TE = {6.5, 13.0, 19.5, 26.0, 32.5} ms, repetition time (TR) = 45 ms, FA(water) = 15°, FA(fat) = 27°—the respective Ernst angles assuming T_1 values of 400 ms and 1400 ms for fat and water respectively—rBW/pixel = 190 Hz and monopolar readout. Parallel imaging acceleration of R = 3 and partial Fourier of 7/8 were applied, resulting in total acquisition time of 4 min 53 s.

2.2.2 | 7T measurements

Sagittal 3D multi-echo GRE SMURF images were acquired with anterior-posterior phase-encoding direction, FOV = 230 × 230 mm, resolution = 1.0 × 1.0 × 1.0 mm, 160 slices, TE = {3.85, 7.70, 11.55, 15.40, 19.25, 23.10} ms, TR = 35 ms, FA(water) = 12°, FA(fat) = 20°—the respective Ernst angles assuming T_1 values of 550 ms and 1700 ms for fat and water respectively—rBW/pixel = 360 Hz, and monopolar readout. Parallel imaging acceleration of R = 3 and partial Fourier of 6/8 were applied, resulting in total acquisition time of 5 min 13 s.

For all volunteers, a low-resolution conventional GRE scan (i.e., with broadband RF excitation) was acquired to calculate the GRAPPA kernel for fat-water separation using parallel imaging reconstruction. The imaging parameters of the prescans were: in-plane resolution = 3.6 × 3.6 mm, TE/TR = 1.5/3.5 ms at 3 T and TE/TR = 3.0/5.4 ms at 7 T, FA = 5°, rBW/pixel = 690 Hz at 3 T and rBW/pixel = 650 Hz at 7 T with the number of slices and slice thickness the same as in the main SMURF scans. To evaluate possible changes to image contrast, signal phase and resulting susceptibility maps from the use of SMURF RF pulses and processing, high-resolution conventional GRE scans, with the same imaging parameters as was used for the SMURF scans, were also acquired and susceptibility maps were calculated as described in the following section (Supporting Figures S1 and S2, which are available online).

2.3 | Data analysis

SMURF fat and water images were reconstructed from raw data in MATLAB (Mathworks Inc, Natick, MA) using slice-GRAPPA[52] and coil-combination with ASPIRE.[53] The fat complex images were corrected for Type 1 (displacement) and Type 2 (phase discrepancy) CSAs and for differences in T_1 and T_2^* relaxation rates (Figure 1). Literature values were used for the T_1 correction (400/1400 ms; and 550/1700 ms for fat/water at 3 and 7 Tesla, respectively).[54-56] For T_2^* correction, separate T_2^* maps of water and fat were generated and the ratio of fat and water signal weighting, in each voxel, was calculated. To avoid transferring noise from this ratio map to the images in a voxel-by-voxel correction, a single correction factor (CF), calculated as the median of the per-voxel ratios of fat and water signal weighting was used. The median was assessed only over voxels for which the fat fraction (FF) was in the range $0.1 \leq FF < 0.8$:

$$CF = median\left(\frac{e^{-TE_{iEcho}/T_{2fat}^*(r)}}{e^{-TE_{iEcho}/T_{2water}^*(r)}}, \text{for all } r, \text{ where } 0.1 < = FF(r) < 0.8\right),$$

and the resulting CF was used for the correction of all mixed voxels.

To generate a head-and-neck mask, maps of temporal phase gradient coherence (Weight 2 in Ref [57,58]) and phase combination quality, i.e., Q-metric,[59] were calculated separately for fat and water. The temporal phase gradient coherence weight, calculated as:

$$C(i,j) = max\left(0, 1 - \left|\Omega\left(\varphi_{i,TE(1)} - \varphi_{j,TE(1)}\right) - \Omega\left(\varphi_{i,TE(2)} - \varphi_{j,TE(2)}\right) \cdot TE(2)/TE(1)\right|\right),$$

with i and j representing two adjacent spatial locations and Ω the wrapping operator, describes how closely the time evolution of phase is to being linear, and the Q-metric, defined as:

$$Q = 100 \times \frac{\left|\sum_{M_c} M_c e^{i\varphi_c}\right|}{\sum_c M_c},$$

with M_c representing the signal acquired by channel c of the receiver array, describes how well the phase offset-corrected signal is matched between the individual receiver channels. Since both of these metrics are low in the voxels with unreliable phase, these voxels tend to be excluded from masks. To exclude voxels with very short relaxation times, the Q-metric of the second echo was used. The fat and water maps of temporal phase gradient coherence (C) were summed to generate a joint fat-water quality map, which was thresholded to exclude voxels with unreliable phase (threshold value of 0.6). The fat and water combination quality (Q) maps were also thresholded (threshold value of 0.98) and combined using an "OR" operation. A joint fat-water mask was generated by combining the maps of temporal phase gradient coherence (C) and the thresholded quality maps (Q) using an "AND" operation (Figure 2). This mask was smoothed (using smoothn in Matlab[60,61]) and thresholded, to fill in small holes and remove small disconnected groups of voxels for example, in the subcranial region (threshold value of 0.6), eroded and
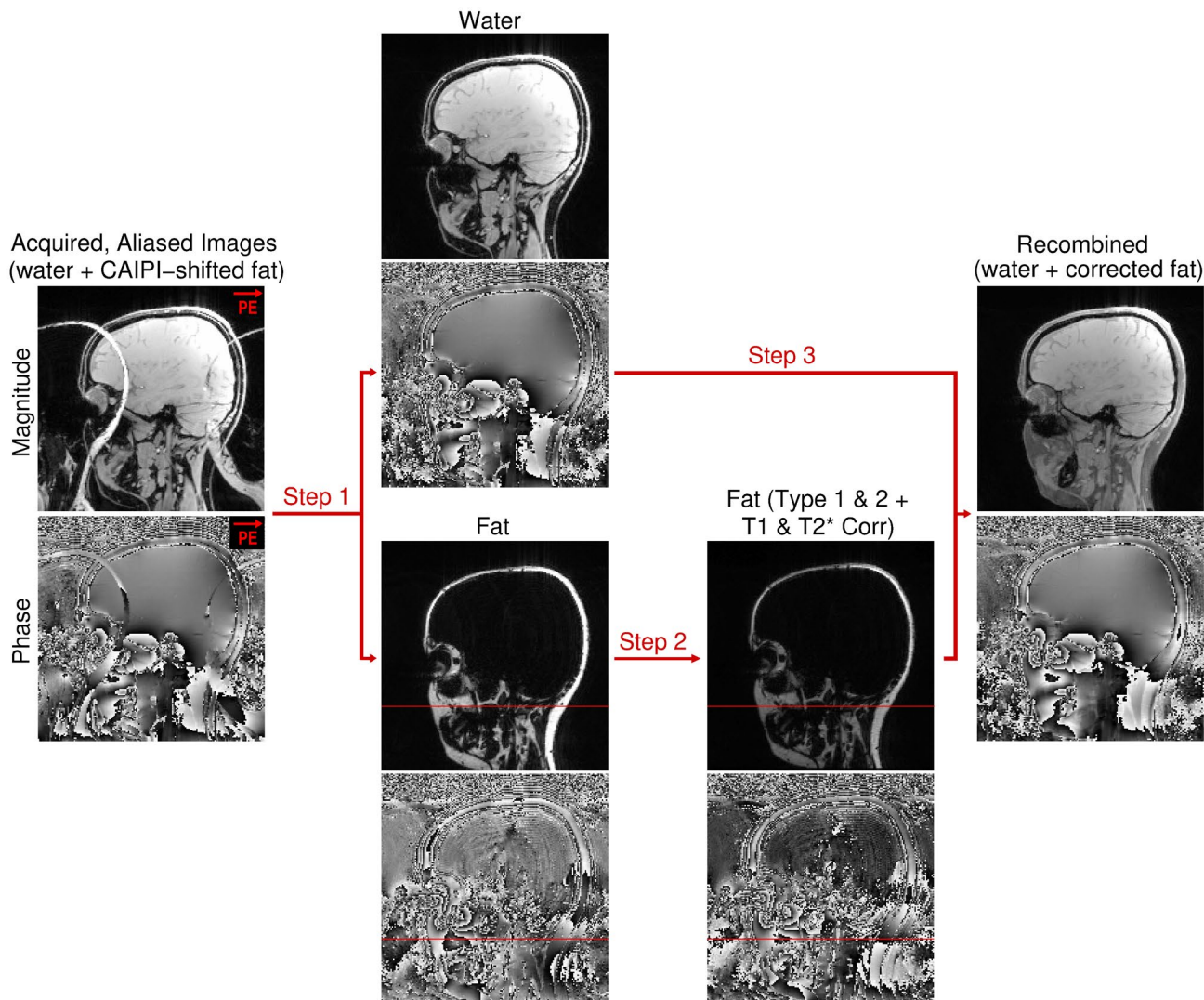
FIGURE 1 Image processing and postprocessing pipeline. In Step 1, overlapping water and CAIPIRINHA-shifted fat images are unaliased using slice-GRAPPA. In Step 2, the fat image is shifted to reverse chemical shift displacement (Type 1 chemical shift artefact)— see the position before and after the correction relative to the red reference line –, corrected for the chemical shift-related phase evolution (Type 2 chemical shift artefact) and rescaled to correct for the bias caused by T_1 and T_2^* relaxation rate differences. In Step 3, the complex fat and water images are recombined, generating a fat-water image free of chemical shift and relaxation rate discrepancies.

filled again (smoothn with subsequent thresholding at 0.3). All threshold values, as well as the combination and order of individual processing steps, were arrived at empirically on the first datasets and used for all volunteers.

To generate susceptibility maps, the multi-echo images were combined over echoes using inverse-variance weighting.[29,62,63] Phase unwrapping was performed using ROMEO.[57,58] Background-field correction was performed with PDF[64] and susceptibility calculation with STAR[65] using the Sepia toolbox.[66]

To assess the need for multi-echo acquisitions, including longer TEs, in QSM imaging of the head-and-neck, QSMs generated from all echoes combined and QSMs generated from individual echoes were compared both qualitatively—by visual assessment of the image contrast,

noise, and presence of artifacts—and quantitatively—via calculation of CNR within ROIs—given as:

$$\text{CNR} = \frac{\left|\text{mean}\left(\text{ROI}_{\text{sig}}\right) - \text{mean}\left(\text{ROI}_{\text{bkg}}\right)\right|}{\text{stdev}\left(\text{ROI}_{\text{noise}}\right)}.$$

Within the brain, the CNR was assessed over eight ROIs located in deep gray matter structures (ROI_{sig}) relative to the neighboring tissue (ROI_{bkg}) and within the neck, over eight ROIs located in fatty structures (ROI_{sig}) relative to the neighboring water-based tissues (ROI_{bkg}). In both cases, the noise was estimated as the standard deviation of the signal within an ROI located in a homogeneous area of white matter ($\text{ROI}_{\text{noise}}$).
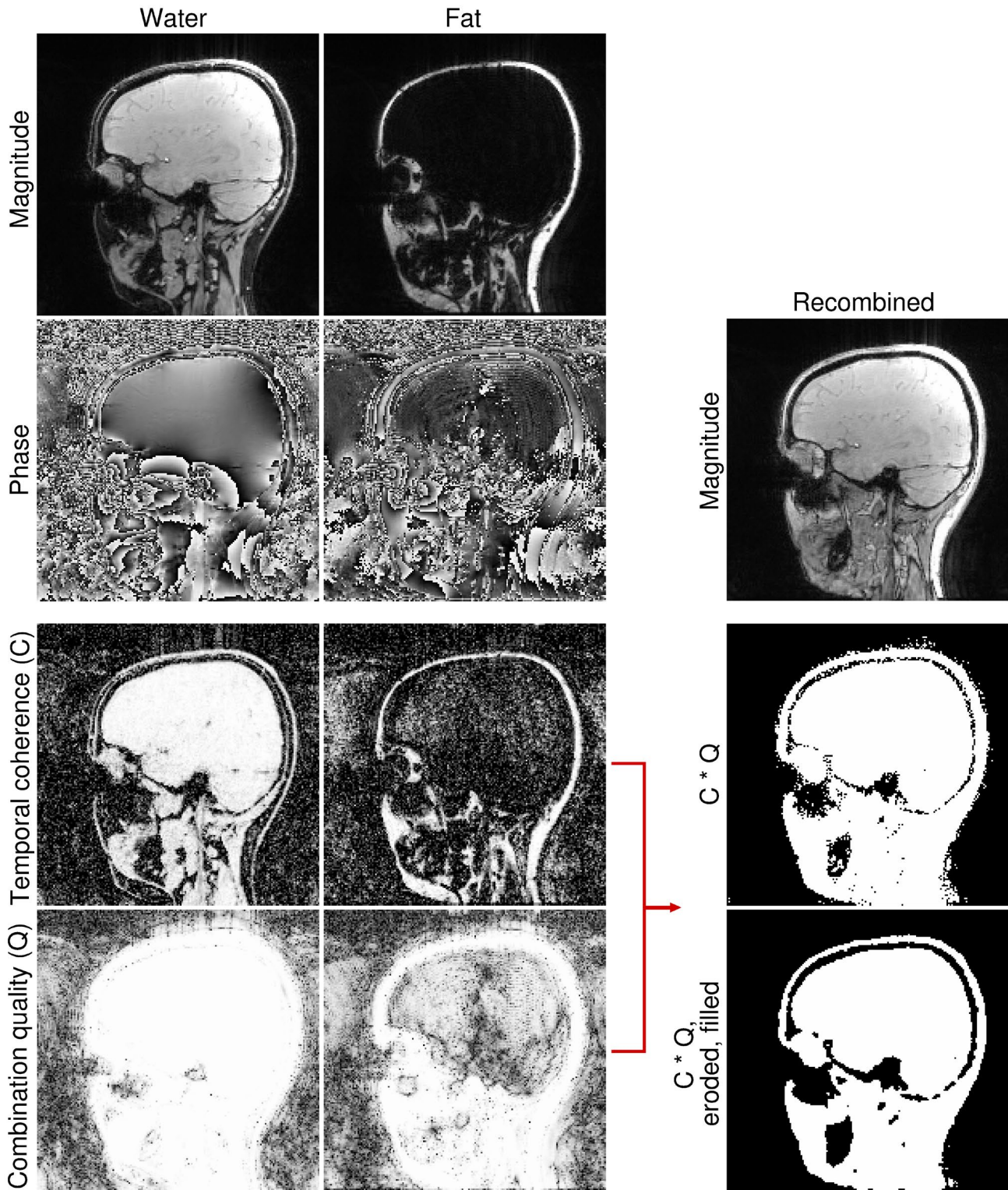
FIGURE 2 The generation of a head-and-neck mask using signal phase. Maps of temporal phase coherence (C) and phase combination quality (Q) are calculated, for fat and water separately, thresholded and combined to generate a single mask (C * Q). This mask is smoothed and thresholded to fill in small holes, eroded, and filled again. Note that the phase combination quality of the second echo is used to exclude voxels with very short relaxation times.

To evaluate the effects of the corrections for CSAs and relaxation rate biases, the susceptibility maps generated from SMURF images with and without the individual corrections were compared both qualitatively—by visual assessment of the correspondence between the location of fatty tissues in the magnitude images and the

paramagnetic areas in the susceptibility maps—and quantitatively—via the standard deviations within 6 ROIs located in areas of homogeneous tissue (i.e., lymph nodes, neck muscles and parotid glands). Additionally, susceptibility values of the fatty tissue were assessed within one extensive ROI, drawn over several distant fatty-neck tissue areas, and compared over the corrections. The quantitative ROI analysis (assessment of CNR, the variance of the susceptibility estimates, and assessment of the susceptibility of fatty tissues) was performed for three 3T volunteers (V1–V3) and three 7T volunteers (V6–V8), and the mean values over volunteers were calculated and compared over the corrections.

3 | RESULTS

There was a very high degree of correspondence between the recombined SMURF fat-water images acquired at the "random" TEs and the conventional images acquired at the same "random" TEs; and between the "random" recombined SMURF fat-water images corrected for the Type 2 CSA and the conventional images acquired at the "in-phase" TEs. This demonstrates that the use of SMURF RF pulses and image reconstruction has no discernible effect on image contrast or signal phase and that the Type 2 CSA correction effectively removed the phase discrepancy between water and fat (Supporting Figures S1 and S2).

The proposed phase-based masking approach, based on the joint fat-water temporal coherence and phase combination quality (Q-metric[59]) effectively excluded noisy phase voxels but retained the voxels in the neck (Figure 2), where, due to decreased coil sensitivities, the magnitude of the signal was lower (mainly at 7 T, because the transmit efficiency of the 32-channel head coil is low in inferior regions, and receive coil coverage of the neck area is limited).

The susceptibility maps generated from the first echo provided good tissue contrast in the areas of short T_2^*, such as the neck and around sinuses, but in the brain, the contrast was low and the maps were noisy (Figure 3A, top row). On the other hand, the susceptibility maps generated from the later echoes showed improved contrast and decreased noise in the brain, but artifacts were present in the neck (Figure 3A, second and third rows). The QSMs generated from all echoes combined showed high contrast and low noise over the entire head-and-neck region (Figure 3A, bottom row). This was confirmed by the quantitative analysis; within the brain, the CNR was higher at the later echoes (Figure 3B, top two rows), but within the neck, the later echoes showed very low CNR and high variance, suggesting unreliability of the results (Figure 3B, bottom two rows). Using all echoes combined

yielded high CNR in all cases. Within the brain ROIs, the CNR peaked, for the 3T acquisition, between the third and fourth echo (TEs of 19.5 ms and 26.0 ms), and for the 7T acquisition, between the fifth and sixth echo (TEs of 19.3 ms and 23.1 ms).

If no Type 1 (displacement) CSA correction was applied, phase unwrapping errors occurred (Figure 4, third row) in areas where the displacement of fat led to signal voids with unreliable phase (Figure 4, second row), causing artifacts in the susceptibility maps (Figure 4, bottom row).

The SMURF method achieved generally well-separated fat and water images of the head-and-neck region at both 3 and 7 Tesla. For some volunteers, the larger field inhomogeneity at 7 T resulted in suboptimal fat-water separation in the very inferior or caudal area of the neck, manifesting as a local loss of water signal and swap of fat signal to the water image or the other way around (depending on the sign of the local field deviation) (Supporting Figure S3). These were generally easy to identify and located outside the area of interest, however.

Figure 5 illustrates the fat-water separation quality achieved by SMURF and the effects of the individual corrections for CSAs and relaxation rate biases on the magnitude, phase, and QSM. Without Type 2 (phase discrepancy) CSA correction (Figure 5, first column), the phase discrepancy between fat and water led to signal cancellation in mixed voxels—'India ink' artifact outlining the fat-water borders. Additionally, the susceptibility values in fatty tissues were higher than with the correction applied. Without the Type 1 (displacement) CSA correction (Figure 5, second column), magnitude images contained areas of fat-water signal overlap as well as signal voids, and susceptibility maps at and around the fat-water borders were blurred and contained artifacts resulting from phase unwrapping errors. These were removed by the application of Type 1 CSA correction (Figure 5, center column). Corrections for fat-water relaxation rate bias (Figure 5, right two columns), primarily in T_1, removed the fat hyperintensity (the fact that the fat signal was disproportionately large compared to the relative proton densities of the fat and water) and, thus, excessive influence on mixed voxels. This resulted in susceptibility maps with a high correspondence between the strongly paramagnetic areas and the locations of fatty tissue structures.

The quantitative analysis also showed that the standard deviation of the QSM values within ROIs, which were located in areas of homogeneous tissue, was reduced when the corrections were applied (Figure 6), with the corrections for Type 1 and Type 2 CSAs having the greatest effects. Without the Type 2 (phase discrepancy) CSA correction, the susceptibility estimates of fatty tissue in the neck were significantly higher than
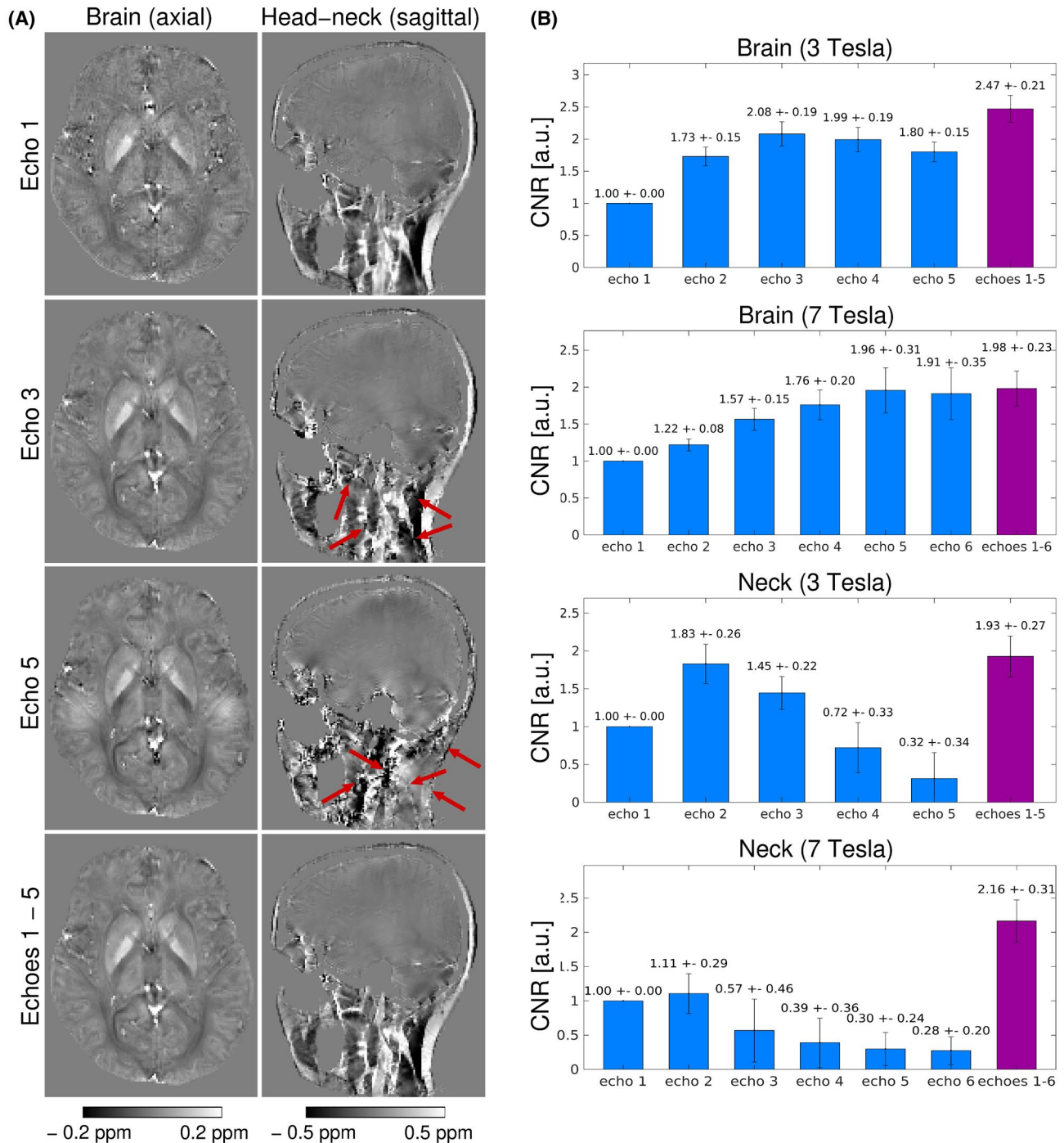
FIGURE 3 Comparison of single-echo and multi-echo susceptibility maps (A) and CNR quantification within the brain and the neck (B). A) 3T QSM images of brain-only (left column) and entire head-and-neck (right column) generated from the first (first row), third (second row), and fifth (third row) echo of the multi-echo acquisition, or from all echoes (bottom row) of the multi-echo acquisition of one 3T volunteer (V1). Note that, while the contrast of the susceptibility maps within the brain visibly increases and the image noise decreases with increasing TE, errors occur for later echoes outside the brain (red arrows). B) Quantification of the CNR within the brain (deep gray matter regions) and within the neck (fatty-neck regions) for the susceptibility maps generated from one respective echo of the multi-echo acquisition. The mean values and standard deviations of the relative CNR values over ROIs are normalized to the CNR of first-echo susceptibility maps and the mean values over the three volunteers (V1–V3 at 3 T and V6–V8 at 7 T) are displayed. While within the brain, the later echoes show higher CNR, in the neck higher CNR is achieved at the earlier echoes. The highest CNR is generally achieved when using all echoes combined.

FIGURE 4 Comparison of phase unwrapping performance when applied to the images recombined without (left column) and with (right column) the correction for the Type 1 (displacement) chemical shift artefact. Note the erroneously unwrapped voxels (third row, red arrows) in the areas, where the displacement of fat results in areas of signal voids (first row) with unreliably defined phase (second row), which lead to artifacts in the susceptibility map (bottom row, red arrows).
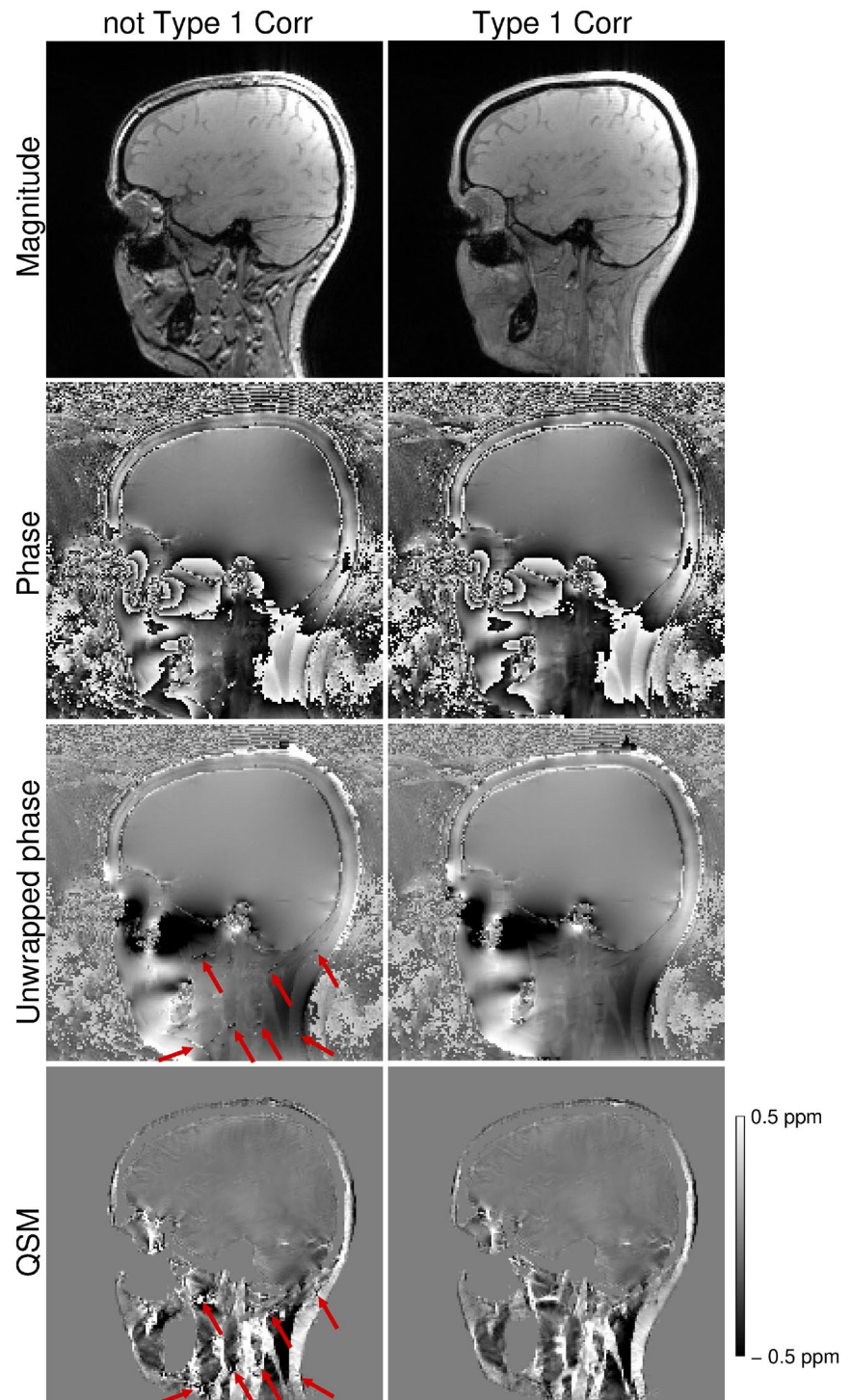
with the correction applied (Figure 7): mean values over the three subjects of 0.97 ppm and 0.54 ppm versus 0.38 ppm and 0.39 ppm at 3 and 7 Tesla, respectively. With all corrections, the susceptibility estimates of fatty neck tissue were 0.41 ppm and 0.40 ppm at 3 and 7 Tesla, respectively.

The estimated T_2^* values of fat and water in mixed voxels were similar (Table 1), resulting in voxel-specific ratios of the signal weightings close to 1. Consequently, the T_2^* bias correction, in which a correction factor,

calculated as a median of these ratios over all mixed voxels was used, had only a modest effect (Figures 5, 8, and 9).

Figures 8,9 and Supporting Figures S4–S13 illustrate the effects of the corrections on susceptibility values for all 3T and 7T volunteers, respectively, and demonstrate that chemical shift artefacts and the bias due to fat-water relaxation differences have to be eliminated to generate susceptibility maps without gross artifacts. Without the Type 2 (phase discrepancy) CSA correction
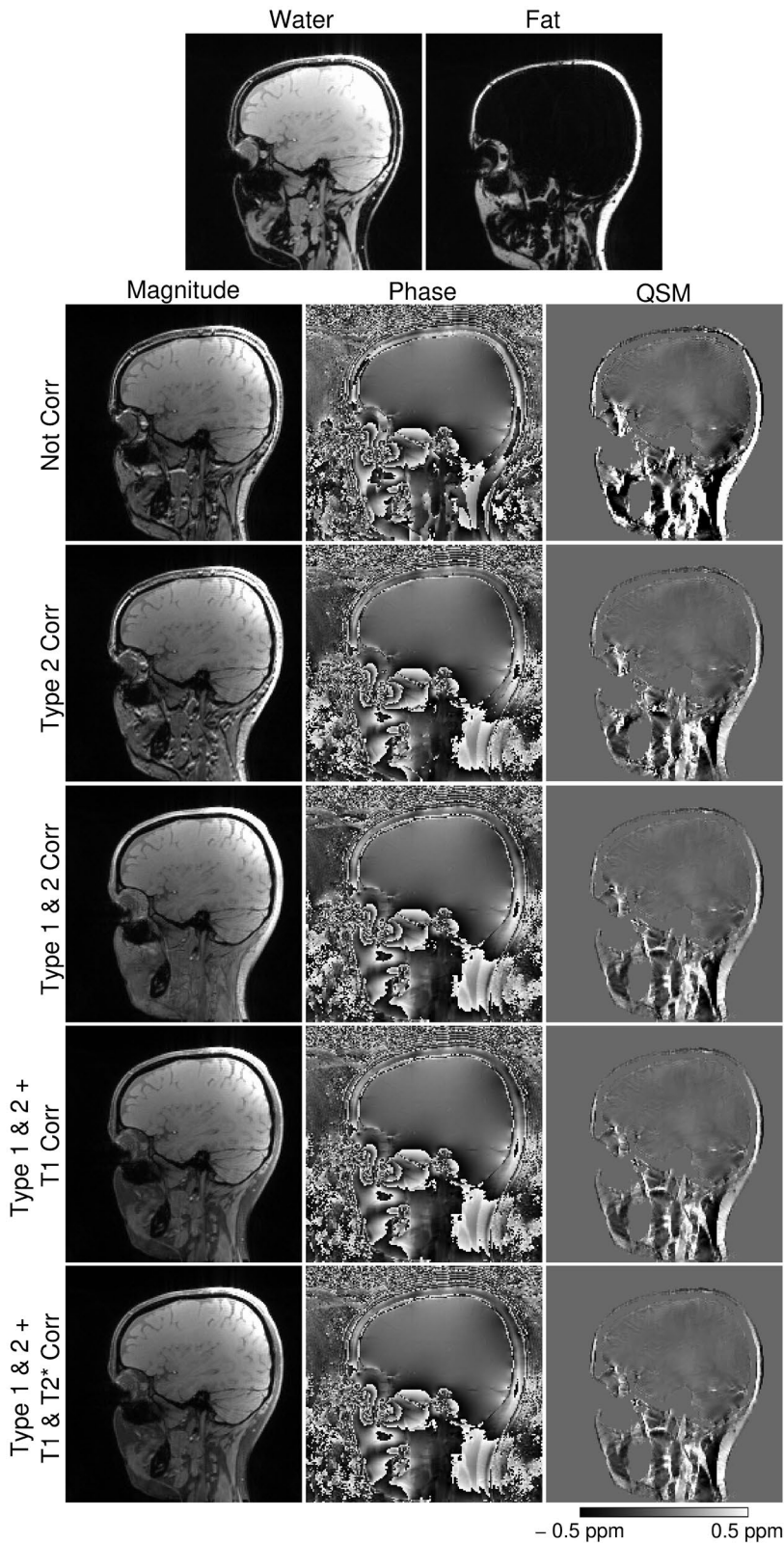
FIGURE 5 Illustration of the effects of corrections for chemical shift artefacts and for bias due to fat-water relaxation rate discrepancy, shown on the magnitude, phase and QSM images of one 3T volunteer (V1). The susceptibility maps generated from the images not corrected for chemical shift effects (row 1) are blurred, and the values are much higher than when corrected for the Type 2 CSA (row 2). The susceptibility maps corrected for the Type 1 and Type 2 CSAs clearly depict the paramagnetic fatty areas (row 3). Corrections for the fat-water differences in T_1 (row 4) and T_2^* (row 5) relaxation rates remove the erroneous domination of fat signal in the mixed voxels. Note the small effect of the T_2^* correction.

(third columns), the susceptibility values of fatty tissues were visibly higher and without the Type 1 (displacement) CSA correction (fourth columns), the susceptibility maps were more blurred around the fat-water borders and contained artifacts resulting from phase unwrapping errors. Corrections for fat-water relaxation rate bias (last two columns), primarily in T_1, removed the excessive influence of fat signal on mixed voxels. With all corrections applied, the susceptibility maps showed a high degree of correspondence between the locations
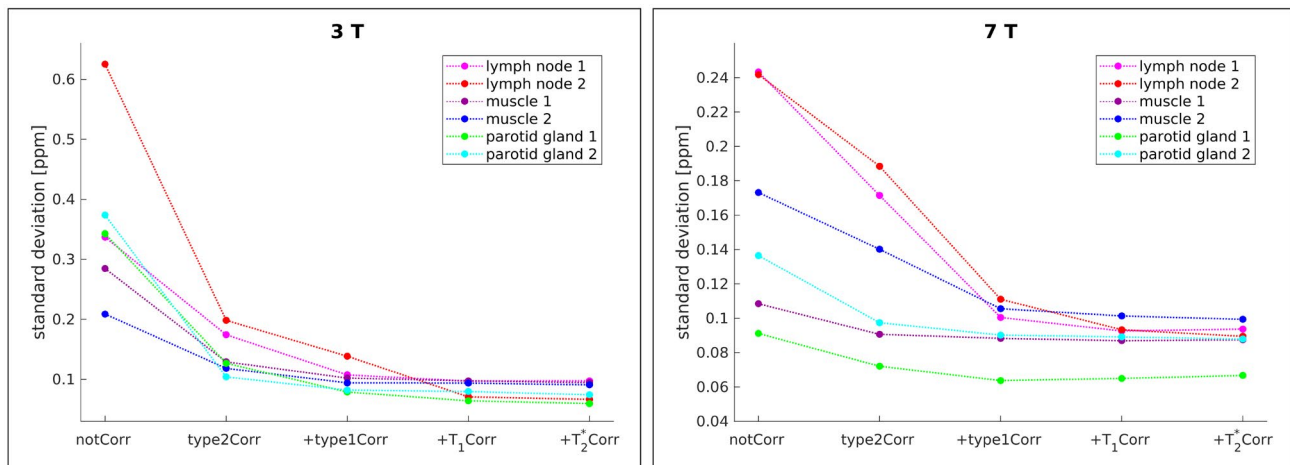
FIGURE 6 Standard deviation of QSM values within ROIs located in areas of homogeneous tissue; mean values over three subjects (V1–V3 and V6–V8 at 3 and 7 Tesla, respectively) are shown. In all ROIs, both at 3 T (left) and 7 T (right), the SD of QSM values is highest when no corrections for the CSAs and relaxation rate biases are applied and decreases with each correction. Note the largest effects attributable to CSA corrections, followed by correction of T_1 bias.
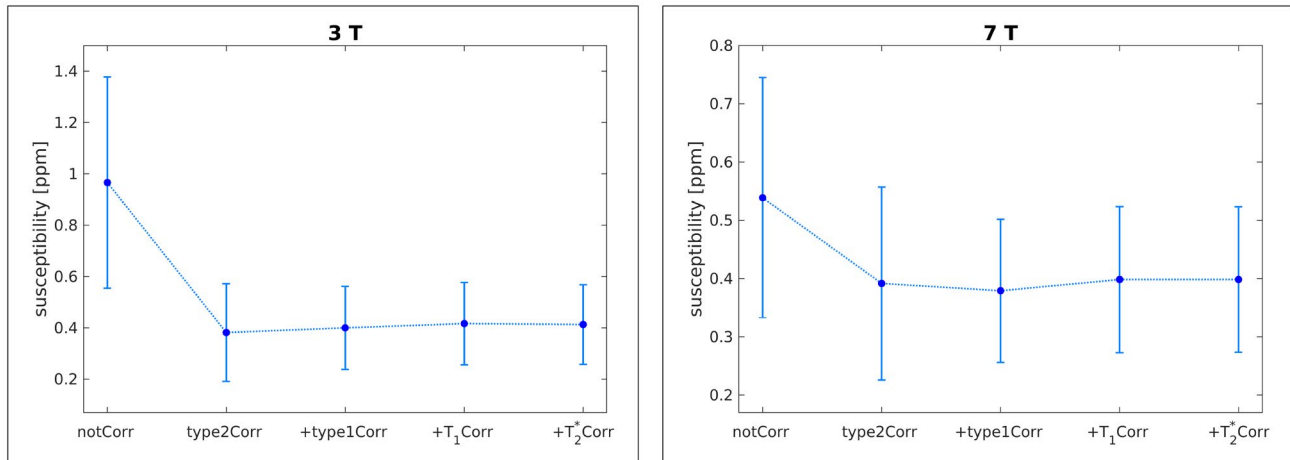

FIGURE 7 Susceptibility estimates of fatty tissue in the neck at 3 T (left) and 7 T (right); mean values over three subjects (V1–V3 and V6–V8 at 3 and 7 Tesla, respectively) are shown. Without correction for the Type 2 (phase discrepancy) chemical shift artefact, the susceptibility estimates are much higher than with the correction, median susceptibilities of 0.97 ppm and 0.54 ppm without corrections versus 0.41 ppm and 0.40 ppm with all corrections applied, at 3 T and 7 T respectively. The variance of the estimates over the ROI is also much higher without the Type 2 CSA correction.

of paramagnetic areas and fatty structures. Note that the application of the corrections significantly improved the quality of the susceptibility maps even in the volunteers with only a small amount of fat in the neck.

4 | DISCUSSION

The challenges of quantitative susceptibility mapping outside of the brain, in regions that typically contain significant amounts of fat, have been addressed using a recently developed Simultaneous Multiple Resonance Frequency (SMURF) imaging approach combined with corrections for chemical shift and relaxation effects and a novel

masking method. This approach led to high-quality susceptibility maps of the entire head-and-neck region, both at 3 and 7 Tesla, with a strong correspondence to the underlying anatomy.

In this study, we adapted the SMURF approach for 7 T, where due to the larger chemical shift difference, shorter RF pulses of 8 ms compared to roughly 12 ms at 3 T, could be used. This allowed a reduction in the minimum TE, roughly 2.5–4.5 ms instead of 4.5–7.0 ms at 3 T (depending on the receiver bandwidth and resolution), and a reduction in echo spacing. The faster-decaying signal at higher field strength could, thus, be captured and high-quality susceptibility maps of the head-and-neck could be generated both at 3 and 7 Tesla. The CNR

T₂* values of fat and water and weighting bias correction factor			
3 Tesla			
	Fat T_2^*	Water T_2^*	T_2^* weighting bias correction factor (echo1/echo2/echo3/echo4/echo5)
V1	17.72	14.80	1.06/1.12/1.19/1.26/1.34
V2	17.83	14.13	1.09/1.19/1.30/1.42/1.55
V3	16.98	15.01	1.06/1.12/1.19/1.25/1.33
V4	12.01	11.77	1.04/1.08/1.12/1.17/1.21
V5	17.81	13.98	1.09/1.19/1.30/1.42/1.55
7 Tesla			
	Fat T_2^*	Water T_2^*	T_2^* weighting bias correction factor (echo1/echo2/echo3/echo4/echo5/echo6)
V6	7.53	8.88	0.93/0.86/0.80/0.75/0.69/0.64
V7	9.62	8.86	1.03/1.07/1.10/1.14/1.18/1.22
V8	9.12	8.58	1.02/1.04/1.07/1.09/1.12/1.14
V9	7.69	8.61	0.95/0.90/0.85/0.81/0.76/0.72
V10	8.79	8.86	0.99/0.98/0.98/0.97/0.96/0.95

TABLE 1 Fat and water T_2^* values and the weighting bias correction factor. Median values over all mixed voxels with fat fractions in the range $0.1 \leq FF < 0.8$ are shown. Note the similarity of T_2^* values of fat and water, resulting in the weighting bias correction factors being close to 1.

of deep gray matter structures peaked, for the 3T measurements, between the third (TE = 19.5 ms) and fourth (TE = 26.0 ms) echo of the five echoes acquired and, for the 7T measurements, between the fifth (TE = 19.3 ms) and sixth (TE = 23.1 ms) echo of the six echoes acquired. This demonstrates that the later echoes are required to achieve high CNR in the brain. On the other hand, in the neck the CNR peaked at the earlier echoes, the second echo at both 3 T (TE = 13.0 ms) and 7 T (TE = 7.7 ms). This shows that, to achieve susceptibility maps with high CNR in the cerebrum, cerebellum, brainstem, as well as in the non-brain regions of the neck, both earlier and later echoes have to be acquired and combined with an effective echo combination approach, such as inverse variance weighting.[29,62,63]

A similar fat-water separation quality was expected to be achieved at 3 and 7 Tesla as both the field inhomogeneity and the chemical shift scale with field strength. In fact, while at 3 T correct fat-water separation was achieved in all cases over the entire head-and-neck (in addition to the subcutaneous region of the caudal neck area of two volunteers), at 7 T, some fat-water swaps occurred in the very inferior or caudal area of the neck for all volunteers. The head-and-neck represents, however, a challenging region in which the numerous interfaces between bones, air in sinuses, ears, and pharynx and soft tissue create strong susceptibility artifacts, leading to difficulties in shimming. In our previous study, well-separated fat and water images of breast, knee, and abdomen could be generated at 3 T.[45] These results for the head-and-neck suggest that advanced shimming methods may be needed to be applied to 7T SMURF imaging of problematic body regions to exploit

the benefits of the inherently higher SNR and shorter required echo trains.

We have shown that the removal of chemical shift artefacts and T_1 relaxation differences is crucial to generating susceptibility maps without gross artifacts, and have demonstrated the sizeable effects of Type 2 (phase discrepancy) CSA and of the often neglected corrections for Type 1 (displacement) CSA and for bias due to fat-water T_1 differences. Despite the absence of a ground truth against which to compare susceptibility estimates, a reduction in the variance over ostensibly homogeneous tissues and improved agreement with literature values points to the effectiveness of the corrections and the veracity of the results. Without the corrections, the susceptibility maps were blurred at fat-water borders and the values were, compared to those in the literature (0.2–0.6 ppm), overestimated (medians of 0.97 ppm and 0.54 ppm for 3 and 7 Tesla, respectively). With the corrections applied, these artifacts were removed (medians of 0.41 ppm and 0.40 ppm for 3 and 7 Tesla, respectively) and a high degree of correspondence was achieved between the location of fatty tissues and the strongly paramagnetic areas of susceptibility maps. Additionally, the standard deviation of susceptibility values across the ROIs located in areas of homogeneous tissue was reduced, suggesting lower levels of noise and artifacts. Although in-phase imaging[12,23,24,26] or the Dixon approach[9,13,25,44] can be used to eliminate Type 2 (phase discrepancy) CSA in QSM, Type 1 (displacement) CSA and T_1 relaxation bias cannot be addressed with those approaches, as explained in the introduction. Chemical shift and relaxation rate effects can be reduced, but not eliminated, using high receiver bandwidths and low flip angles, but this comes at the price of decreased SNR. With SMURF,
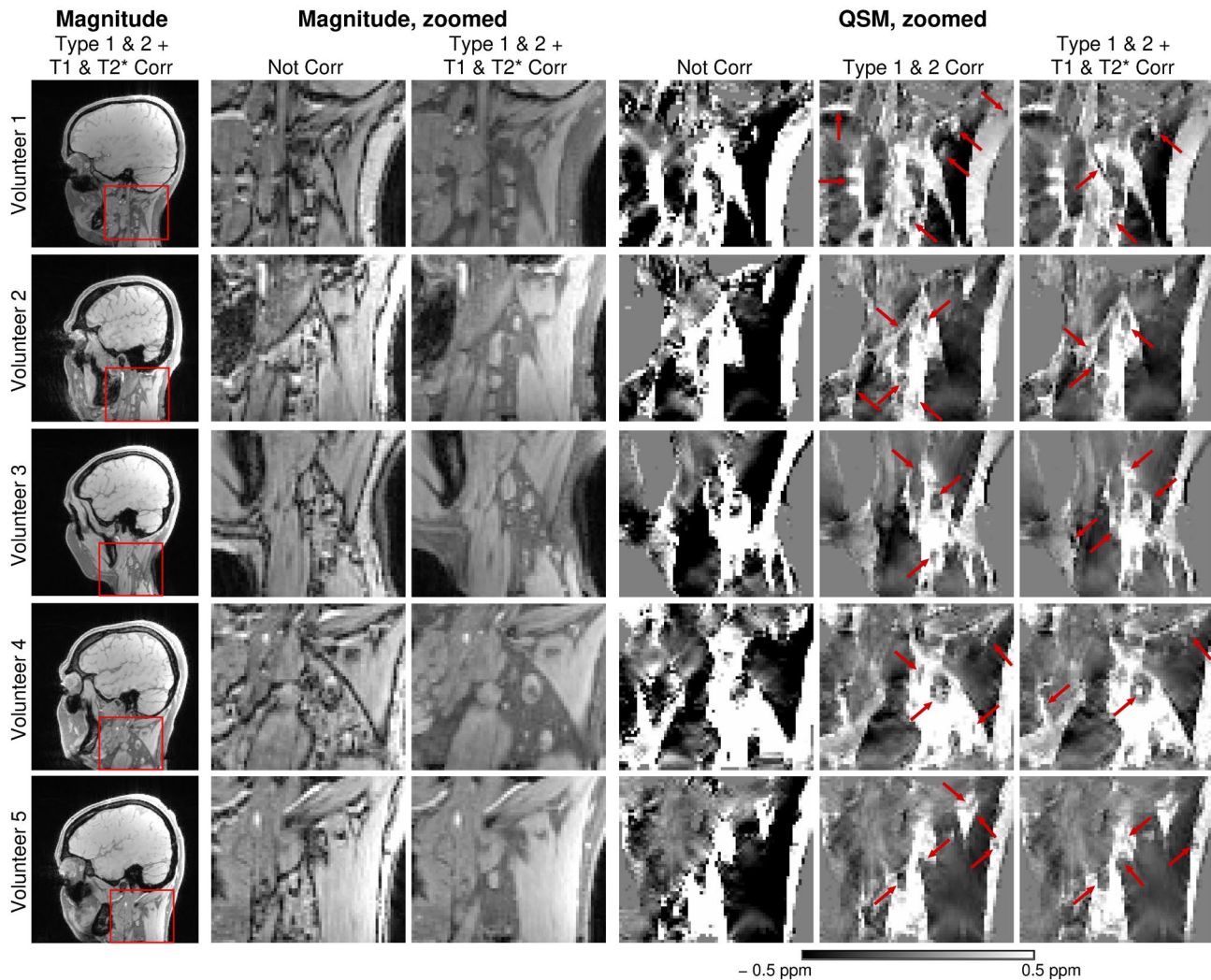
FIGURE 8 Susceptibility maps of all 3T volunteers (V1–V5) generated without any correction and with the corrections for chemical shift artefacts and bias due to fat-water relaxation rate discrepancies applied. Without the corrections (column 4), the susceptibility maps are blurred and the values are, compared to literature values, overestimated. The susceptibility maps corrected for the Type 1 and Type 2 CSA clearly depict the paramagnetic fatty areas (column 5, red arrows). Corrections for the fat-water differences in T_1 and T_2^* relaxation rates remove the dominant influence of fat in the mixed voxels (column 6, red arrows).

Type 1 and Type 2 chemical shift artefacts and T_1 relaxation bias could be corrected and artifact-free susceptibility maps of the head-and-neck could be generated.

In this work, the T_1 bias correction was performed using literature values of fat and water and led to QSMs with better correspondence to the underlying anatomy. Alternatively, and more precisely, T_1 mapping could be carried out and measured T_1 values could be used for correction. This would eliminate the need for the assumption that T_1 values are the same for all water-based and all fat-based tissues present in the mixed voxels, but would require T_1 mapping to be performed for both fat and water.

The T_2^* values of fat and water in mixed voxels were shown to be quite similar, leading to correction factors for the disparate T_2^* weighting of fat and water signals, which were close to 1. The similarity in fat-water T_2^* values suggests, given the known differences in their T_2 (48 ms and 29 ms, and 46 ms and 23 ms for fat and water at 3 and 7 Tesla, respectively),[55] that the field inhomogeneity contribution dominates over the T_2 contribution to T_2^*. This concurs with observed T_2^* estimates in mixed voxels (at 3 T, of 16 ms and 14 ms for fat and water respectively, and at 7 T, of 9 ms for both) being much lower than the literature T_2 values. Although this disparity is generally increased for later echoes, later echoes contributed little to the combined phase, and thereby also to the QSMs, because of short T_2^* constants and inverse-variance weighting. The effect of the T_2^* correction on susceptibility maps was correspondingly small.

The proposed masking approach, which is based on the signal phase, specifically, the product of temporal phase coherence and phase combination quality (Q-metric), was shown to provide a simple means of generating a
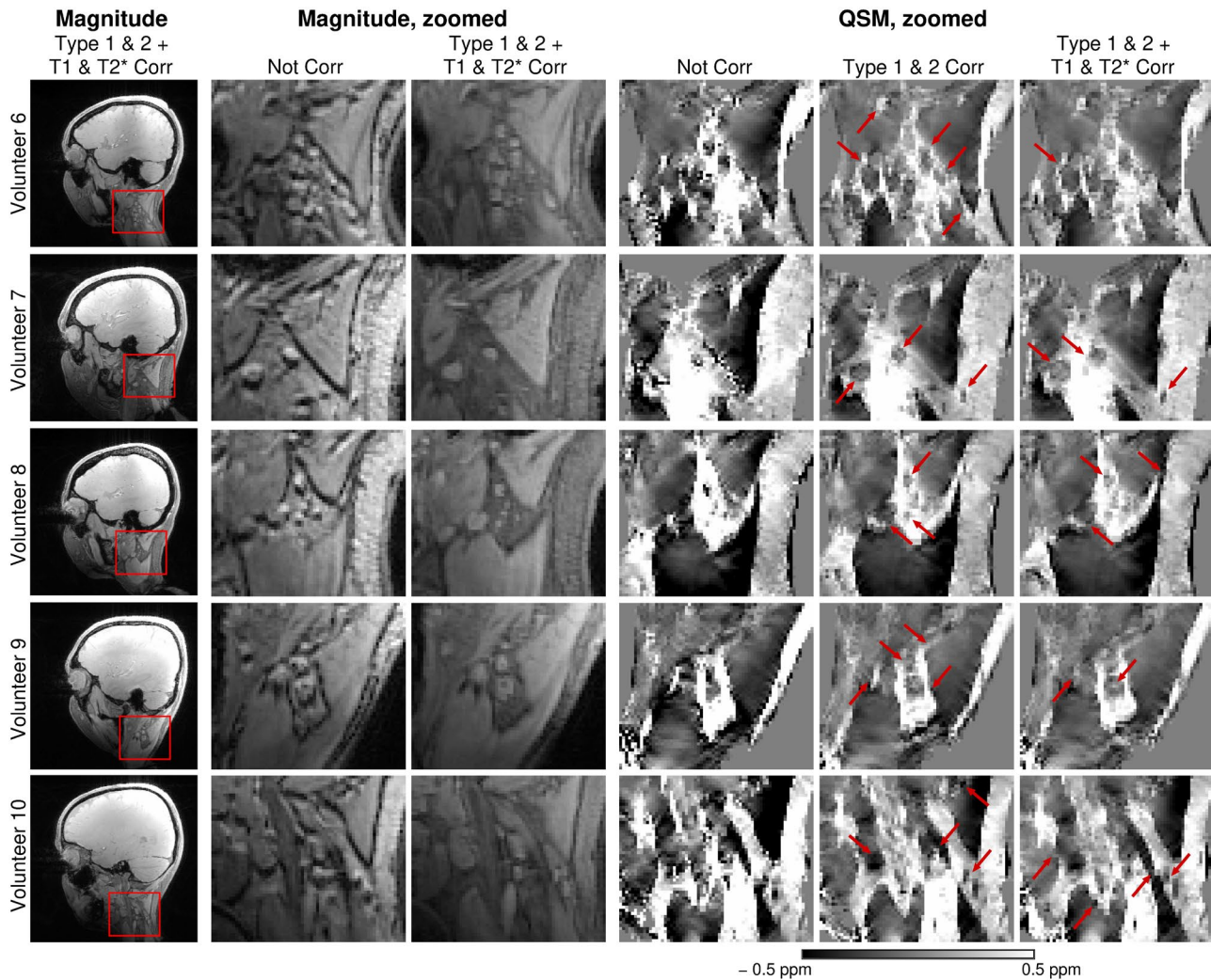
FIGURE 9 Susceptibility maps of all 7T volunteers (V6–V10) generated without any correction and with the corrections for chemical shift artefacts and bias due to fat-water relaxation rate discrepancies applied. Without the corrections (column 4), the susceptibility maps are blurred and the values are, compared to literature values, overestimated. The susceptibility maps corrected for the Type 1 and Type 2 CSA clearly depict the paramagnetic fatty areas (column 5, red arrows). Corrections for the fat-water differences in T_1 and T_2^* relaxation rates remove the dominant influence of fat in the mixed voxels (column 6, red arrows).

head-and-neck mask. A similar phase-based approach has been adopted by Stewart et al,[46] who used thresholded spatial phase coherence. In the presence of fat, however, the spatial coherence would be low at the fat-water borders due to the fat-water phase discrepancy resulting from their susceptibility differences. Although this approach could be applied to the fat and water images separately, the values would be low at tissue edges. In both cases, using spatial phase coherence would, thus, lead to the exclusion of voxels at the fat-water border. Similarly, if the temporal phase coherence were to be calculated directly for the combined fat-water image, the resulting temporal phase coherence maps would be low at the fat-water borders, because of the fat-water susceptibility difference leading to a different temporal evolution of fat and water phase signal. The border voxels would be, thus, excluded from the mask even if

Type 2 CSA correction or in-phase acquisition would be used (Supporting Figure S14). To avoid excluding these voxels from the mask, the temporal phase coherence maps of the separated fat and water signals had to be calculated and then combined. The proposed approach was shown to generate a mask that included most of the anatomy of interest and excluded noisy voxels. Nevertheless, if masks were to be needed in more problematic areas still, such as the hearing nerve in a study of acoustic neuroma, for instance, SMURF could be combined with a total-field inversion (TFI) QSM approach.[25,67]

As demonstrated in this study, SMURF opens up an alternative approach to QSM outside the brain. In addition to the head-and-neck region, SMURF could be also used for chemical shift and relaxation bias-free susceptibility mapping of the liver, kidney, joints, breast, spine,

and other organs and regions. Although in-phase imaging[12,23,24,26] and Dixon imaging[9,13,25,44] are often used in these cases to remove Type 2 (phase discrepancy) CSA, we have shown that the correction of Type 1 (displacement) CSA and also of the bias due to fat-water relaxation differences, which cannot be performed with those approaches, is required for accurate susceptibility mapping. Additionally, to reduce shading artifacts, separate susceptibility maps for fat and water could be calculated separately from SMURF images and then combined.[17] This would, however, make the approach more sensitive to masking and would benefit from, and likely be dependent upon, a TFI approach. Recently, a new preconditioned water-fat TFI (wfTFI) algorithm[68] was developed and used to reduce background field-removal artifacts, noise amplification, and streaking artifacts in QSM of water-fat regions. A graph-cut[25] (Dixon style) approach was used to separate water and fat and to generate a fieldmap and an R_2^* map, which were then used as the basis for the QSM inversion. Potentially, SMURF could be also combined with wfTFI, which would also allow Type 2 CSA and relaxation bias to be eliminated.

In addition to GRE-based QSM of non-brain regions, SMURF would also bring benefits to QSM of the brain performed with EPI-based sequences. EPI and 3D EPI, in particular, are attracting increasing interest in QSM due to acquisition speed and the possibility to simultaneously map structure and function.[69-74] In EPI, however, the low receiver bandwidth along the phase-encoding direction results in a large chemical shift displacement of the fat signal, which can shift fat from the skull into the brain and subcutaneous fat in the neck such that it overlays inferior brain regions such as the brainstem. Fat-suppression could be used, although the high specific absorption rate (SAR) demand of fat-sat pulses at ultrahigh field (UHF) make fat-water imaging an appealing solution[75] and one that would retain fat information for QSM of non-brain regions and also possibly allow the use of fat images as navigators for prospective motion correction[76] and dynamic B_0 shimming.[77]

We have shown that CSAs and relaxation rate biases, that adversely affect the reliability of QSM in fatty regions, can be reduced using fat-water imaging with SMURF. This approach was shown to generate high-quality susceptibility maps of the head-and-neck at 3 and 7 Tesla with a strong correspondence to the known anatomy.

5 | CONCLUSIONS

The challenges of QSM outside of the brain, in regions that typically contain significant amounts of fat, have been addressed with SMURF fat-water imaging with corrections for Type 1 and Type 2 CSAs and for relaxation rate biases. Unlike conventional imaging with broadband excitation, this approach was shown to be required to generate susceptibility maps of fatty regions without gross artifacts and with high correspondence between the paramagnetic areas and the locations of fatty tissues.

DATA AVAILABILITY STATEMENT
The data that support the findings of this study, including the ROIs, are openly available in "3T SMURF-based QSM data" and "7T SMURF-based QSM data" https://doi.org/10.7910/DVN/IEFCRA at and https://doi.org/10.7910/DVN/4HBJC6, references [78] and [79], respectively.

ORCID
Beata Bachrata https://orcid.org/0000-0002-3352-8966
Siegfried Trattnig https://orcid.org/0000-0003-1623-3303
Simon Daniel Robinson https://orcid.org/0000-0001-7463-5162

TWITTER
Simon Daniel Robinson @simon_mri

REFERENCES
1. Shmueli K, de Zwart JA, van Gelderen P, Li TQ, Dodd SJ, Duyn JH. Magnetic susceptibility mapping of brain tissue in vivo using MRI phase data. *Magn Reson Med.* 2009;62:1510-1522.
2. Schweser F, Robinson SD, de Rochefort L, Li W, Bredies K. An illustrated comparison of processing methods for phase MRI and QSM: removal of background field contributions from sources outside the region of interest. *NMR Biomed.* 2017;30:e3604.
3. Wang Y, Liu T. Quantitative susceptibility mapping (QSM): decoding MRI data for a tissue magnetic biomarker. *Magn Reson Med.* 2015;73:82-101.
4. Wang YI, Spincemaille P, Liu Z, et al. Clinical quantitative susceptibility mapping (QSM): Biometal imaging and its emerging roles in patient care: clinical QSM Biometals. *J Magn Reson Imaging.* 2017;46:951-971.
5. Ravanfar P, Loi SM, Syeda WT, et al. Systematic review: Quantitative Susceptibility Mapping (QSM) of brain iron profile in neurodegenerative diseases. *Front Neurosci.* 2021;15.
6. Vinayagamani S, Sheelakumari R, Sabarish S, et al. Quantitative susceptibility mapping: technical considerations and clinical applications in neuroimaging. *J Magn Reson Imaging.* 2021;53:23-37.

7. Sharma SD, Fischer R, Schoennagel BP, et al. MRI-based quantitative susceptibility mapping (QSM) and R2* mapping of liver iron overload: comparison with SQUID-based biomagnetic liver susceptometry: QSM and R2*: comparison With SQUID. *Magn Reson Med*. 2017;78:264-270.

8. Sharma SD, Hernando D, Horng DE, Reeder SB. Quantitative Susceptibility Mapping in the abdomen as an imaging biomarker of hepatic iron overload. *Magn Reson Med*. 2015;74:673-683.

9. Dong J, Liu T, Chen F, et al. Simultaneous phase unwrapping and removal of chemical shift (SPURS) using graph cuts: application in quantitative susceptibility mapping. *IEEE Trans Med Imaging*. 2015;34:531-540.

10. Li J, Lin H, Liu T, et al. Quantitative susceptibility mapping (QSM) minimizes interference from cellular pathology in R2* estimation of liver iron concentration. *J Magn Reson Imaging*. 2018;48:1069-1079.

11. Jafari R, Sheth S, Spincemaille P, et al. Rapid automated liver quantitative susceptibility mapping. *J Magn Reson Imaging*. 2019;50:725-732.

12. Schweser F, Herrmann K-H, Deistung A, et al. Quantitative magnetic susceptibility mapping (QSM) in breast disease reveals additional information for MR-based characterization of carcinoma and calcification. *Proceedings of the 19th Annual Meeting of ISMRM*. , 2011. #1014.

13. Dimov AV, Liu T, Spincemaille P, et al. Joint estimation of chemical shift and quantitative susceptibility mapping (chemical QSM). *Magn Reson Med*. 2015;73:2100-2110.

14. Xie L, Dibb R, Cofer GP, et al. Susceptibility tensor imaging of the kidney and its microstructural underpinnings. *Magn Reson Med*. 2015;73:1270-1281.

15. Straub S, Laun FB, Emmerich J, et al. Potential of quantitative susceptibility mapping for detection of prostatic calcifications. *J Magn Reson Imaging*. 2017;45:889-898.

16. Straub S, Emmerich J, Schlemmer H-P, et al. Mask-adapted background field removal for artifact reduction in quantitative susceptibility mapping of the prostate. *Tomography*. 2017;3:96-100.

17. Sato R, Shirai T, Soutome Y, Bito Y, Ochi H. Quantitative susceptibility mapping of prostate with separate calculations for water and fat regions for reducing shading artifacts. *Magn Reson Imaging*. 2020;66:22-29.

18. Dibb R, Qi Y, Liu C. Magnetic susceptibility anisotropy of myocardium imaged by cardiovascular magnetic resonance reflects the anisotropy of myocardial filament alpha-helix polypeptide bonds. *J Cardiovasc Magn Reson*. 2015;17:60.

19. Dibb R, Xie L, Wei H, Liu C. Magnetic susceptibility anisotropy outside the central nervous system. *NMR Biomed*. 2017;30.

20. Wen Y, Nguyen TD, Liu Z, et al. Cardiac quantitative susceptibility mapping (QSM) for heart chamber oxygenation. *Magn Reson Med*. 2018;79:1545-1552.

21. Wei H, Dibb R, Decker K, et al. Investigating magnetic susceptibility of human knee joint at 7 Tesla. *Magn Reson Med*. 2017;78:1933-1943.

22. Diefenbach MN, Meineke J, Ruschke S, Baum T, Gersing A, Karampinos DC. On the sensitivity of quantitative susceptibility mapping for measuring trabecular bone density. *Magn Reson Med*. 2019;81:1739-1754.

23. Guo Y, Liu Z, Wen Y, et al. Quantitative susceptibility mapping of the spine using in-phase echoes to initialize inhomogeneous field and R2* for the nonconvex optimization problem of fat-water separation. *NMR Biomed*. 2019;32:e4156.

24. Karsa A, Punwani S, Shmueli K. An optimized and highly repeatable MRI acquisition and processing pipeline for quantitative susceptibility mapping in the head-and-neck region. *Magn Reson Med*. 2020;84:3206-3222.

25. Boehm C, Diefenbach MN, Makowski MR, Karampinos DC. Improved body quantitative susceptibility mapping by using a variable-layer single-min-cut graph-cut for field-mapping. *Magn Reson Med*. 2021;85:1697-1712.

26. Buch S, Liu S, Ye Y, Cheng Y-CN, Neelavalli J, Haacke EM. Susceptibility mapping of air, bone, and calcium in the head. *Magn Reson Med*. 2015;73:2185-2194.

27. Ruetten PPR, Cluroe AD, Usman A, Priest AN, Gillard JH, Graves MJ. Simultaneous MRI water-fat separation and quantitative susceptibility mapping of carotid artery plaque pre- and post-ultrasmall superparamagnetic iron oxide-uptake. *Magn Reson Med*. 2020;84:686-697.

28. Ikebe Y, Ishimaru H, Imai H, et al. Quantitative susceptibility mapping for carotid atherosclerotic plaques: a pilot study. *Magn Reson Med Sci*. 2020;19:135-140.

29. Bachrata B, Eckstein K, Trattnig S, Robinson SD. QSM of the head-and-neck at 7T using simultaneous fat-water imaging with SMURF. *Proceedings of the 29th Annual Meeting of ISMRM. Virtual Conference*, 2021. #0795.

30. Deistung A, Schäfer A, Schweser F, et al. High-resolution MR imaging of the human brainstem in vivo at 7 Tesla. *Front Hum Neurosci*. 2013;7:710.

31. Elias GJB, Loh A, Gwun D, et al. Deep brain stimulation of the brainstem. *Brain*. 2021;144:712-723.

32. Mazzone P, Vilela Filho O, Viselli F, et al. Our first decade of experience in deep brain stimulation of the brainstem: elucidating the mechanism of action of stimulation of the ventrolateral pontine tegmentum. *J Neural Transm*. 2016;123:751-767.

33. Eskreis-Winkler S, Deh K, Gupta A, et al. Multiple sclerosis lesion geometry in quantitative susceptibility mapping (QSM) and phase imaging. *J Magn Reson Imaging*. 2015;42:224-229.

34. Karsa A. *Optimising MRI Magnetic Susceptibility Mapping for Applications in Challenging Regions of the Body*. University College London; 2018. https://discovery.ucl.ac.uk/id/eprint/10064348/. Accessed September 16, 2021.

35. Ren J, Dimitrov I, Sherry AD, Malloy CR. Composition of adipose tissue and marrow fat in humans by 1H NMR at 7 Tesla. *J Lipid Res*. 2008;49:2055-2062.

36. Spincemaille P, Anderson J, Wu G, et al. Quantitative Susceptibility Mapping: MRI at 7T versus 3T. *J Neuroimaging*. 2020;30:65-75.

37. Reeder SB, Hu HH, Sirlin CB. Proton density fat-fraction: a standardized mr-based biomarker of tissue fat concentration. *J Magn Reson Imaging*. 2012;36:1011-1014.

38. Yang IY, Cui Y, Wiens CN, Wade TP, Friesen-Waldner LJ, McKenzie CA. Fat fraction bias correction using T1 estimates and flip angle mapping. *J Magn Reson Imaging*. 2014;39:217-223.

39. Yu H, McKenzie CA, Shimakawa A, et al. Multiecho reconstruction for simultaneous water-fat decomposition and T2* estimation. *J Magn Reson Imaging*. 2007;26:1153-1161.

40. Dixon WT. Simple proton spectroscopic imaging. *Radiology*. 1984;153:189-194.

41. Pineda AR, Reeder SB, Wen Z, Pelc NJ. Cramér-Rao bounds for three-point decomposition of water and fat. *Magn Reson Med*. 2005;54:625-635.

42. Reeder SB, McKenzie CA, Pineda AR, et al. Water–fat separation with IDEAL gradient-echo imaging. *J Magn Reson Imaging*. 2007;25:644-652.

43. Wu B, Li W, Avram AV, Gho SM, Liu C. Fast and tissue-optimized mapping of magnetic susceptibility and T2* with multi-echo and multi-shot spirals. *NeuroImage*. 2012;59:297-305.

44. Liu J, Christiansen SD, Drangova M. Single multi-echo GRE acquisition with short and long echo spacing for simultaneous quantitative mapping of fat fraction, B0 inhomogeneity, and susceptibility. *NeuroImage*. 2018;172:703-717.

45. Bachrata B, Strasser B, Bogner W, et al. Simultaneous Multiple Resonance Frequency imaging (SMURF): Fat-water imaging using multi-band principles. *Magn Reson Med*. 2021;85:1379-1396.

46. Stewart AW, Robinson SD, O'Brien K, et al. QSMxT: robust masking and artefact reduction for quantitative susceptibility mapping. *bioRxiv*. Published online May 6, 2021:2021.05.05.442850.

47. Shinnar M, Eleff S, Subramanian H, Leigh JS. The synthesis of pulse sequences yielding arbitrary magnetization vectors. *Magn Reson Med*. 1989;12:74-80.

48. Le Roux P. Exact synthesis of radio frequency waveforms. In: *Proceedings of the 7th Annual Meeting of SMRM*, San Francisco, CA, USA. 1988;1049.

49. Pauly J, Le Roux P, Nishimura D, Macovski A. Parameter relations for the Shinnar-Le Roux selective excitation pulse design algorithm. *IEEE Trans Med Imaging*. 1991;10:53-65.

50. Soher BJ, Semanchuk P, Todd D, Steinberg J. VeSPA: Integrated applications for RF pulse design, spectral simulation and MRS data analysis. In: *Proceedings of the 19th Annual Meeting of ISMRM*. Montreal, Quebec, Canada, 2011. #1410.

51. Accessed September 16, 2021. https://vespa-mrs.github.io/vespa.io/

52. Setsompop K, Gagoski BA, Polimeni JR, Witzel T, Wedeen VJ, Wald LL. Blipped-Controlled Aliasing in Parallel Imaging (blipped-CAIPI) for simultaneous multi-slice EPI with reduced g-factor penalty. *Magn Reson Med*. 2012;67:1210-1224.

53. Eckstein K, Dymerska B, Bachrata B, et al. Computationally efficient combination of multi-channel phase data from multi-echo acquisitions (ASPIRE). *Magn Reson Med*. 2018;79: 2996-3006.

54. Gold GE, Han E, Stainsby J, Wright G, Brittain J, Beaulieu C. Musculoskeletal MRI at 3.0 T: relaxation times and image contrast. *Am J Roentgenol*. 2004;183:343-351.

55. Jordan CD, Saranathan M, Bangerter NK, Hargreaves BA, Gold GE. Musculoskeletal MRI at 3.0T and 7.0T: a comparison of relaxation times and image contrast. *Eur J Radiol*. 2013;82:734-739.

56. Rooney WD, Johnson G, Li X, et al. Magnetic field and tissue dependencies of human brain longitudinal 1H2O relaxation in vivo. *Magn Reson Med*. 2007;57:308-318.

57. Dymerska B, Eckstein K, Bachrata B, et al. Phase unwrapping with a rapid opensource minimum spanning tree algorithm (ROMEO). *Magn Reson Med*. 2021;85:2294-2308.

58. Accessed September 16, 2021. https://github.com/korbinian90/ROMEO

59. Robinson S, Grabner G, Witoszynskyj S, Trattnig S. Combining phase images from multi-channel RF coils using 3D phase

60. Garcia D. smoothn. Accessed September 16, 2021. https://de.mathworks.com/matlabcentral/fileexchange/25634-smoothn

61. Garcia D. Robust smoothing of gridded data in one and higher dimensions with missing values. *Comput Stat Data Anal*. 2010;54:1167-1178.

62. Eckstein K, Bachrata B, Hangel G, et al. Improved susceptibility weighted imaging at ultra-high field using bipolar multi-echo acquisition and optimized image processing: CLEAR-SWI. *NeuroImage*. 2021;237:118175.

63. Quinn MP, Gati JS, Klassen LM, et al. Comparison of multiecho postprocessing schemes for SWI with use of linear and nonlinear mask functions. *Am J Neuroradiol*. 2014;35:38-44.

64. Liu T, Khalidov I, de Rochefort L, et al. A novel background field removal method for MRI using projection onto dipole fields (PDF). *NMR Biomed*. 2011;24:1129-1136.

65. Li W, Wang N, Yu F, et al. A method for estimating and removing streaking artifacts in quantitative susceptibility mapping. *NeuroImage*. 2015;108:111-122

66. Chan K-S, Marques JP. SEPIA-Susceptibility mapping pipeline tool for phase images. *NeuroImage*. 2020;227:117611.

67. Liu Z, Kee Y, Zhou D, Wang Y, Spincemaille P. Preconditioned total field inversion (TFI) method for quantitative susceptibility mapping. *Magn Reson Med*. 2017;78:303-315.

68. Boehm C, Sollmann N, Meineke J, et al. Preconditioned water-fat total field inversion: application to spine quantitative susceptibility mapping. *Magn Reson Med*. 2022;87:417-430.

69. Langkammer C, Bredies K, Poser BA, et al. Fast quantitative susceptibility mapping using 3D EPI and total generalized variation. *NeuroImage*. 2015;111:622-630.

70. Sun H, Wilman AH. Quantitative susceptibility mapping using single-shot echo-planar imaging: Echo-Planar Quantitative Susceptibility Mapping. *Magn Reson Med*. 2015;73:1932-1938.

71. Sun H, Seres P, Wilman AH. Structural and functional quantitative susceptibility mapping from standard fMRI studies: QSM from fMRI studies. *NMR Biomed*. 2017;30:e3619.

72. Tourell M, Jin J, Stewart A, et al. Submillimeter, sub-minute quantitative susceptibility mapping using a multi-shot 3D-EPI with 2D CAIPIRINHA acceleration. In: *Proceedings of the 29th Annual Meeting of ISMRM. Virtual Conference*, 2021. #0787.

73. Bachrata B, Eckstein K, Trattnig S, Robinson SD. Considerations in quantitative susceptibility mapping using echo planar imaging. *Proceedings of the 26th Annual Meeting of ISMRM*. Paris, France, 2018. #4996.

74. Ehrmann A, Bachrata B, Eckstein K, et al. Fast, high resolution QSM of the brainstem at 7T using super-resolution 2D EPI. In: *Proceedings of the 28th Annual Meeting of ISMRM. Virtual Conference*. 2020. #3785.

75. Seginer A, Furman-Haran E, Goldberg I, Schmidt R. Lipid and water separation through an SMS-like approach in 7T to reduce SAR in brain EPI. *Proceedings of the 29th Annual Meeting of ISMRM*. Virtual Conference, 2021. #0891.

76. Skare S, Hartwig A, Mårtensson M, Avventi E, Engström M. Properties of a 2D fat navigator for prospective image domain correction of nodding motion in brain MRI. *Magn Reson Med*. 2015;73:1110-1119.

77. Gretch F, Kober T, Waszak M, Marques JP, Gallichan D. High temporal resolution retrospective motion and B0 correction

using FIDNavs and segmented FatNavs at 7 T. *Proceedings of the 24th Annual Meeting of ISMRM*. Singapore, 2016. #4251.

78. Bachrata B. 3T SMURF-based QSM data. Harvard Dataverse, V1. 2021. https://doi.org/10.7910/DVN/IEFCRA

79. Bachrata B. 7T SMURF-based QSM data. Harvard Dataverse, V1. 2021. https://doi.org/10.7910/DVN/4HBJC6

SUPPORTING INFORMATION

Additional supporting information may be found in the online version of the article at the publisher's website.

FIGURE S1 Comparison of conventional GRE images (i.e. with broadband RF excitation) with recombined SMURF images at 3 Tesla. There is a very high degree of correspondence between the conventional image acquired at "random" echo-times (first row) and the recombined SMURF fat-water image acquired at the same, "random" echo-times (second row), demonstrating that the use of SMURF RF pulses and image reconstruction has no discernible effect on image contrast, signal phase or resulting susceptibility maps. Similarly, there was a high degree of correspondence between the conventional image acquired at the "in-phase" echo times (third row) and the "random" recombined SMURF fat-water image corrected for the Type 2 chemical shift artefact (fourth row), demonstrating that the correction effectively removed the phase discrepancy between water and fat

FIGURE S2 Comparison of conventional GRE images (i.e. with broadband RF excitation) with recombined SMURF images at 7 Tesla. There is a very high degree of correspondence between the conventional image acquired at "random" echo-times (first row) and the recombined SMURF fat-water image acquired at the same, "random" echo-times (second row), demonstrating that the use of SMURF RF pulses and image reconstruction has no discernible effect on image contrast, signal phase or resulting susceptibility maps. Similarly, there was a high degree of correspondence between the conventional image acquired at the "in-phase" echo times (third row) and the "random" recombined SMURF fat-water image corrected for the Type 2 chemical shift artefact (fourth row), demonstrating that the correction effectively removed the phase discrepancy between water and fat

FIGURE S3 Fat-water separation errors in the head-and-neck SMURF imaging. At 3 Tesla (left), in two out of five volunteers, fat and water signals are swapped in a small area of the very caudal, subcutaneous neck region. At 7 Tesla (right), in all five volunteers some local fat-water swaps are visible—either also in the very caudal, subcutaneous neck region (V6 and V10) or in the very inferior neck region. The swaps are, however, easy to identify and localized mostly outside the region of interest

FIGURE S4 Susceptibility maps of one 3T volunteer (V1) generated without any correction and with the individual corrections for chemical shift artefacts and relaxation rate bias applied. Without the corrections (row 3), the susceptibility maps are blurred and the values are much higher than when corrected for the Type 2 CSA (row 4). The susceptibility maps corrected for the Type 1 and Type 2 CSA clearly depict the paramagnetic fatty areas (row 5, red arrows). Corrections for the fat-water differences in T_1 (row 6) and T_2^* (row 7) relaxation rates remove the dominant influence of fat in the mixed voxels (row 6, red arrows). Note the small effect of the T_2^* correction

FIGURE S5 Susceptibility maps of one 3T volunteer (V2) generated without any correction and with the individual corrections for chemical shift artefacts and relaxation rate bias applied. Without the corrections (row 3), the susceptibility maps are blurred and the values are much higher than when corrected for the Type 2 CSA (row 4). The susceptibility maps corrected for the Type 1 and Type 2 CSA clearly depict the paramagnetic fatty areas (row 5, red arrows). Corrections for the fat-water differences in T_1 (row 6) and T_2^* (row 7) relaxation rates remove the dominant influence of fat in the mixed voxels (row 6, red arrows). Note the small effect of the T_2^* correction

FIGURE S6 Susceptibility maps of one 3T volunteer (V3) generated without any correction and with the individual corrections for chemical shift artefacts and relaxation rate bias applied. Without the corrections (row 3), the susceptibility maps are blurred and the values are much higher than when corrected for the Type 2 CSA (row 4). The susceptibility maps corrected for the Type 1 and Type 2 CSA clearly depict the paramagnetic fatty areas (row 5, red arrows). Corrections for the fat-water differences in T_1 (row 6) and T_2^* (row 7) relaxation rates remove the dominant influence of fat in the mixed voxels (row 6, red arrows). Note the small effect of the T_2^* correction

FIGURE S7 Susceptibility maps of one 3T volunteer (V4) generated without any correction and with the individual corrections for chemical shift artefacts and relaxation rate bias applied. Without the corrections (row 3), the susceptibility maps are blurred and the values are much higher than when corrected for the Type 2 CSA (row 4). The susceptibility maps corrected for the Type 1 and Type 2 CSA clearly depict the paramagnetic fatty areas (row 5, red arrows). Corrections for the fat-water differences in T_1 (row 6) and T_2^* (row 7) relaxation rates remove the dominant influence of fat in the mixed voxels (row 6, red arrows). Note the small effect of the T_2^* correction

FIGURE S8 Susceptibility maps of one 3T volunteer (V5) generated without any correction and with the individual corrections for chemical shift artefacts and relaxation rate bias applied. Without the corrections (row 3), the susceptibility maps are blurred and the values are much higher than when corrected for the Type 2 CSA (row 4). The

susceptibility maps corrected for the Type 1 and Type 2 CSA clearly depict the paramagnetic fatty areas (row 5, red arrows). Corrections for the fat-water differences in T_1 (row 6) and T_2^* (row 7) relaxation rates remove the dominant influence of fat in the mixed voxels (row 6, red arrows). Note the small effect of the T_2^* correction

FIGURE S9 Susceptibility maps of one 7T volunteer (V6) generated without any correction and with the individual corrections for chemical shift artefacts and relaxation rate bias applied. Without the corrections (row 3), the susceptibility maps are blurred and the values are much higher than when corrected for the Type 2 CSA (row 4). The susceptibility maps corrected for the Type 1 and Type 2 CSA clearly depict the paramagnetic fatty areas (row 5, red arrows). Corrections for the fat-water differences in T_1 (row 6) and T_2^* (row 7) relaxation rates remove the dominant influence of fat in the mixed voxels (row 6, red arrows). Note the small effect of the T_2^* correction

FIGURE S10 Susceptibility maps of one 7T volunteer (V7) generated without any correction and with the individual corrections for chemical shift artefacts and relaxation rate bias applied. Without the corrections (row 3), the susceptibility maps are blurred and the values are much higher than when corrected for the Type 2 CSA (row 4). The susceptibility maps corrected for the Type 1 and Type 2 CSA clearly depict the paramagnetic fatty areas (row 5, red arrows). Corrections for the fat-water differences in T_1 (row 6) and T_2^* (row 7) relaxation rates remove the dominant influence of fat in the mixed voxels (row 6, red arrows). Note the small effect of the T_2^* correction

FIGURE S11 Susceptibility maps of one 7T volunteer (V8) generated without any correction and with the individual corrections for chemical shift artefacts and relaxation rate bias applied. Without the corrections (row 3), the susceptibility maps are blurred and the values are much higher than when corrected for the Type 2 CSA (row 4). The susceptibility maps corrected for the Type 1 and Type 2 CSA clearly depict the paramagnetic fatty areas (row 5, red arrows). Corrections for the fat-water differences in T_1 (row 6) and T_2^* (row 7) relaxation rates remove the dominant influence of fat in the mixed voxels (row 6, red arrows). Note the small effect of the T_2^* correction

FIGURE S12 Susceptibility maps of one 7T volunteer (V9) generated without any correction and with the individual

corrections for chemical shift artefacts and relaxation rate bias applied. Without the corrections (row 3), the susceptibility maps are blurred and the values are much higher than when corrected for the Type 2 CSA (row 4). The susceptibility maps corrected for the Type 1 and Type 2 CSA clearly depict the paramagnetic fatty areas (row 5, red arrows). Corrections for the fat-water differences in T_1 (row 6) and T_2^* (row 7) relaxation rates remove the dominant influence of fat in the mixed voxels (row 6, red arrows). Note the small effect of the T_2^* correction

FIGURE S13 Susceptibility maps of one 7T volunteer (V10) generated without any correction and with the individual corrections for chemical shift artefacts and relaxation rate bias applied. Without the corrections (row 3), the susceptibility maps are blurred and the values are much higher than when corrected for the Type 2 CSA (row 4). The susceptibility maps corrected for the Type 1 and Type 2 CSA clearly depict the paramagnetic fatty areas (row 5, red arrows). Corrections for the fat-water differences in T_1 (row 6) and T_2^* (row 7) relaxation rates remove the dominant influence of fat in the mixed voxels (row 6, red arrows). Note the small effect of the T_2^* correction

FIGURE S14 The performance of the proposed masking approach when applied to the separated fat and water images (left two columns) and to the combined fat-water image (right column). The temporal coherence map of the recombined fat-water image shows low values in the mixed voxels at the fat-water borders, resulting in an exclusion of most of the mixed voxels of interest from the head-and-neck mask (right column, bottom). A joint temporal coherence map generated from the combination of separate fat and water temporal coherence maps shows high coherence values in mixed voxels, leading to these voxels being retained (middle column, bottom)

Supplementary Material